Electronic Supplementary Material (ESI) for Journal of Materials Chemistry A.
This journal is © The Royal Society of Chemistry 2022

Supporting Information

Tracking the Nanoparticle Exsolution/Reoxidation processes of Ni-doped $SrTi_{0.3}Fe_{0.7}O_{3-\delta}$ electrodes for Intermediate Temperature Symmetric Solid Oxide Fuel Cells

Mariano Santaya,*[a] Catalina Elena Jiménez,**[b] Horacio Esteban Troiani,[a,c,d] Emilia Andrea Carbonio,[b,e] Mauricio Damián Arce,[a,b] Lucia Maria Toscani,[a,f] Raul Garcia-Diez,[b] Regan George Wilks,[b] Axel Knop-Gericke,[e,g] Marcus Bär,[b,h,i] and Liliana Verónica Mogni [a,d]

[a.] *Departamento Caracterización de Materiales, INN-CNEA-CONICET, Av. Bustillo 9500, Bariloche, Rio Negro, 8400, Argentina.*
[b.] *Helmholtz-Zentrum Berlin für Materialien und Energie GmbH, Albert-Einstein-Str.15, 12489, Berlin, Germany*
[c.] *Universidad Nacional de Río Negro, Río Negro, Argentina*
[d.] *Instituto Balseiro, Universidad Nacional de Cuyo, R8402AGP San Carlos de Bariloche, Argentina*
[e.] *Fritz-Haber Institute, Dept. of Inorganic Chemistry, Faradayweg 4, 14195 Berlin, Germany*
[f.] *Instituto de Tecnologías Emergentes y Ciencias Aplicadas (ITECA), UNSAM-CONICET, Escuela de Ciencia y Tecnología, Laboratorio de Cristalografía Aplicada, Av. 25 de Mayo 1169, 1650 San Martín, Provincia De Buenos Aires, Argentina*
[g.] *MPI for Chemical Energy Conversion, Stiftstrasse 34 – 36, 45470 Mülheim an der Ruhr, Germany*
[h.] *Friedrich Alexander Universität Erlangen-Nürnberg, Egerlandstr. 3, 91058 Erlangen, Germany*
[i.] *Helmholtz Institute Erlangen-Nürnberg for Renewable Energy (HI ERN), Albert-Einstein.Str. 15, 12489 Berlin, Germany*
* Corresponding author1: marianosantaya@gmail.com
** Corresponding author2: catalina.jimenez@helmholtz-berlin.de

S1. Complementary thermochemical analysis

Figure S1 shows the Temperature Programed Reduction for STF and STFN pristine powders under a 5% dry H_2 atmosphere. Both measurements were collected using 35 mg powder samples obtained by the sol-gel route. The peak at 350 °C was assigned to the Fe cation partial reduction in the perovskite and is present in both samples.[1] This process is similar to the mass evolution in TG analysis at 700 °C when the atmosphere is changed to Ar, and to the first reduction step in wet H_2 atmosphere (Figure 1.a). Peaks at 393 and 434 °C can be associated to the formation of exsolved Ni-Fe nanoparticles in agreement with TG long-term evolution of reduction. Under this dry H_2 atmosphere samples are unstable and decompose above 750 °C. Reduction of some Ti^{4+} to Ti^{3+} reduction cannot be excluded in the region between 600-700 °C.

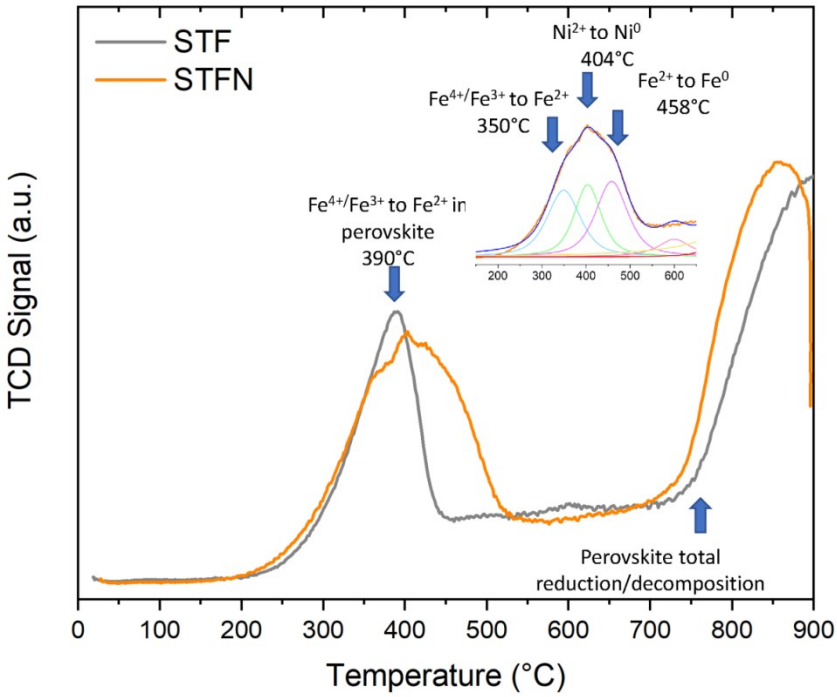

Figure S1 Temperature Programed Reduction profiles (5% dry H_2/Ar balance) measured with a thermal conductivity detector (TCD) for STF and STFN pristine powders. The processes assigned to each peak are indicated on the graphic.

S2. Complementary microstructural characterization.

The XRD diffraction patterns shown in Figure S2 confirm the perovskite cubic structure for the STFN electrode, which is preserved after reduction at 700 °C in a wet 50% H_2 atmosphere and after reoxidation in air. The figure also shows the presence of secondary phases: in the pristine case, a small NiO phase corresponding to Ni that is not incorporated into the perovskite during synthesis, and in the reduced case, the formation of a phase compatible with a FCC Ni-Fe alloy after exsolution (estimated from the lattice parameter as ~$Ni_{0.56}Fe_{0.44}$, according to Vegard's law).[2,3]

Figure S3 shows a SEM-EDS mapping of the STFN pellet after reduction at 700 °C and 50%H_2/47%N_2/3%H_2O. Exsolved NP can be seen although the EDS spatial resolution is not enough to identify their composition, which was done with TEM-EDS as in Figure 1.c. The presence of isolated Ni particles that were not incorporated to the material during the synthesis can also be observed: these particles are responsible for the small NiO phase in the XRD pristine pellet of Figure S2. We can see that the oxygen (O Kα1) map presents lower intensity in the region over these particles, indicating that they are reduced to Ni^0 in this reducing condition.

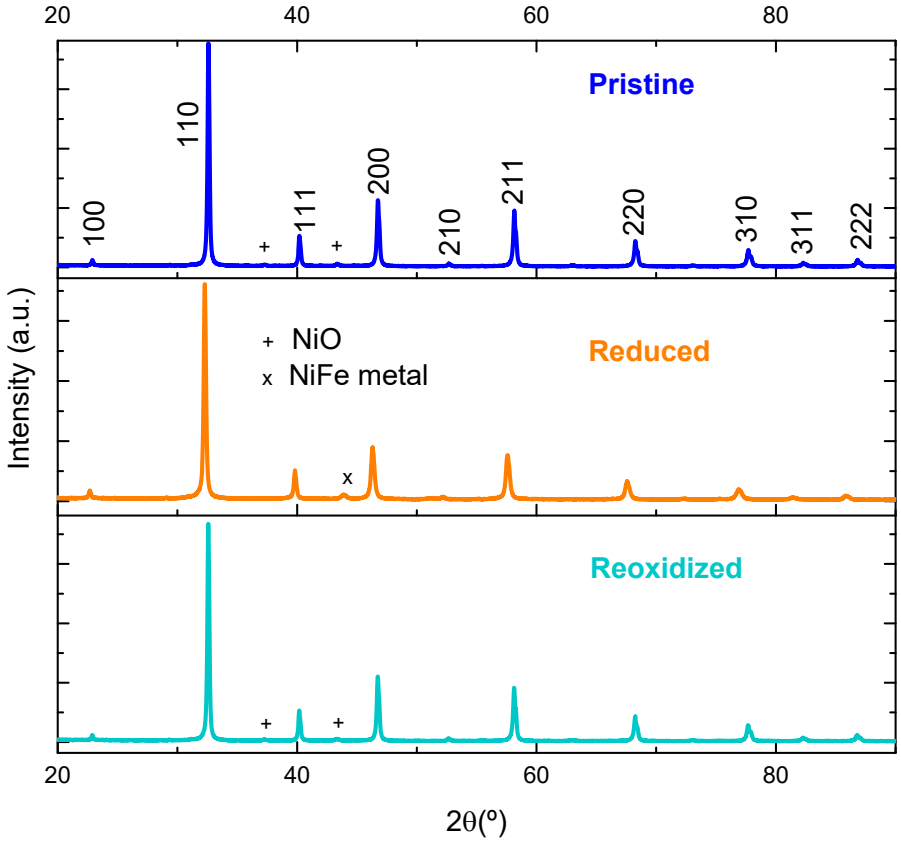

Figure S2 XRD data of the STFN powder (a) pristine, (b) after reduction at 700 ºC in a wet 50% H_2 atmosphere and (c) after 24 h reoxidation at 700 ºC in air.

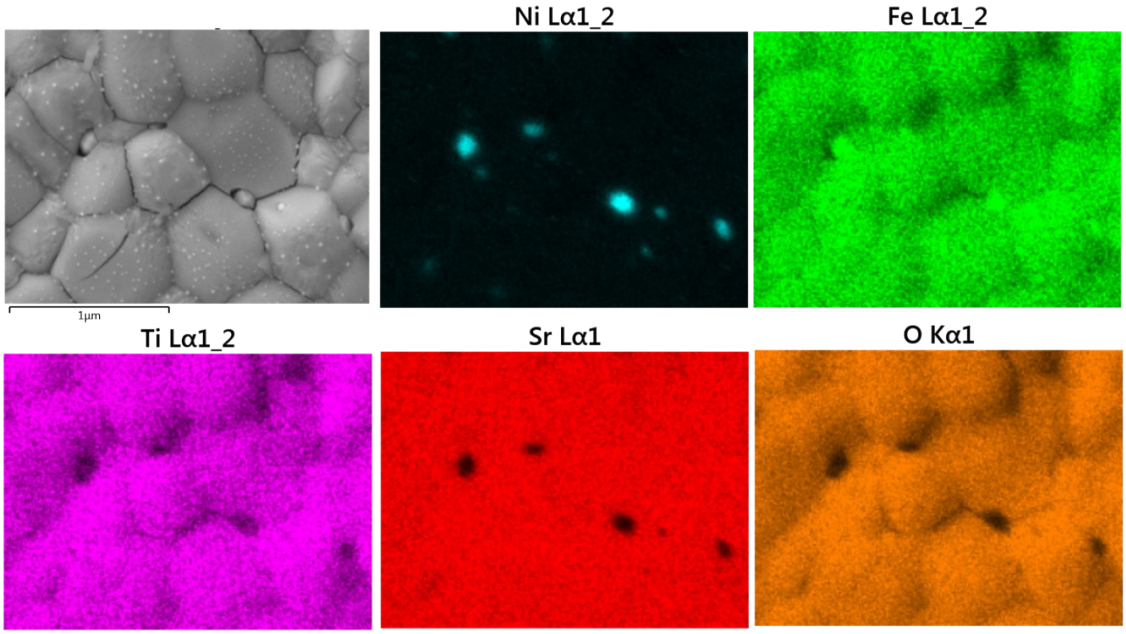

Figure S3. SEM-EDS mapping of the STFN pellet after reduction at 700 °C in a 50%H_2/47%N_2/3%H_2O atmosphere.

S3. Complementary electrochemical analysis

Figure S4 shows the Nyquist plots of the EIS spectra measured for the symmetrical cell with STFN electrodes at different temperatures, first as (a) cathode in pristine conditions, raising temperature from 500 °C to 700 °C, then (b) as anode in 10%H_2/3%H_2O/87%Ar atmosphere, dropping temperature from 700 °C to 500 °C, and finally (c) as cathode in reoxidized conditions (air atmosphere) raising temperature from 500 °C to 700 °C.

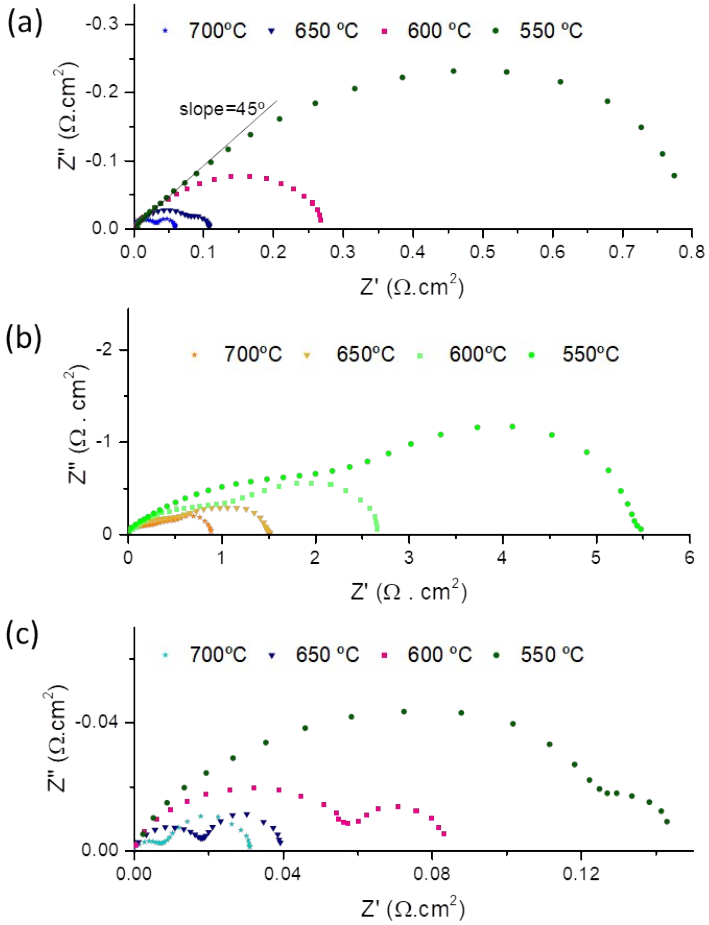

Figure S4. Nyquist plots of the EIS spectra for the symmetrical cell with STFN electrodes measured as (a) cathode in cathode in pristine conditions, (b) as anode in 10%H2/3%H2O/87%Ar atmosphere, and (c) as cathode in reoxidized conditions.

Figure S5 shows the comparison between the EIS spectra acquired in air and pure O_2. The low frequency arc almost vanishes at high pO_2, and the high frequency response reduces its resistance from 0.357 Ω cm² to 0.174 Ω cm², which matches with a ~$pO_2^{-0.44}$ dependence.

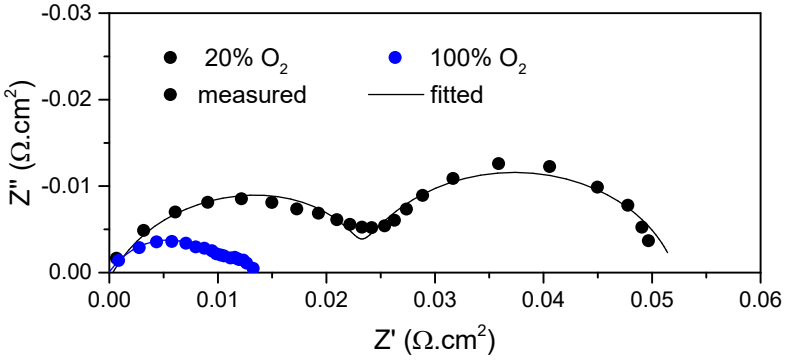

Figure S5. Nyquist plot of the STFN cell measured with a gas flow rate of 100 ml min^{-1} and a O_2/Ar mixture of 20% and 100% O_2.

As mentioned in the main text, all of the spectra in this work were fitted combining R/CPE and Gerischer circuit elements. The expression for the R/CPE element used is given by [4]:

$$Z = R\frac{1}{1 + R\,Q\,(j\,\omega)^n}$$

where R is the resistance, j is the imaginary unit, ω is the angular frequency and the capacitance was estimated from

$$C = \frac{(Q\,R)^{1/n}}{R}$$

For the Gerischer element the impedance was expressed as:

$$Z_G = R_G\frac{1}{(1 + \tau_G\,j\,\omega)^n}$$

where τ_G is the Gerischer element time constant, and the capacitance was estimated from the fitting parameters as $C_G = \tau_G/R_G$, according to references [5,6].

S4. Complementary NAP-XPS /NAP-XAS analysis

S4.1. Binding energy shift estimation

There is an energy shift clearly observed in the E_b of the NAP-XPS spectra, between oxidizing and reducing atmospheres due to a shift of the Fermi level linked to the variation of O_2 molar fraction in each atmospheres.[7,8] The shift can be estimated by calculating the theoretical open circuit voltage of a fuel cell U_{cell} operating at 700 °C and 0.5 mbar of air (20% O_2/80% N_2) in the cathode and 50% H_2/47% N_2/3% H_2O in the anode, which is related to the differences in oxygen chemical potential in both atmospheres, according to Equation S1:

$$U_{cell} = \left|\frac{\Delta\mu_{O_2}}{4F}\right| \qquad \text{(S1)}$$

Then, the $\Delta\mu_{O_2}$ at the studied conditions can be calculated accordingly by:

i) Calculating the O_2 molar fraction (x_{O_2}) on each atmosphere. For the oxidizing atmosphere is straightforward, however, in the case of the reducing atmosphere the water equilibrium must be considered. For this, one can use the following thermodynamic cycle:

$$H_2 + \frac{1}{2}O_2 \xrightarrow{1\,T_1 \to\, 298\,K} H_2 + \frac{1}{2}O_2 \xrightarrow{2.\,P_1 \to 1atm} H_2 + \frac{1}{2}O_2 \xrightarrow{3.\ 298K,\,1atm} (H_2O)_{liq} \xrightarrow{4.\,298K \to\, 373K}$$

$$\xrightarrow{4.\,298K \to\, 373K} (H_2O)_{liq} \xrightarrow{5.vap} (H_2O)_{vap} \xrightarrow{6.373K \to\, T_1} (H_2O)_{vap} \xrightarrow{7,1atm \to\, P_1} (H_2O)_{vap}$$

Tabulated values of enthalpies and entropies of formation for each species (for instance for water, H^o_{fH2O} and S^o_{fH2O}), and heat capacities C_{pi} for the different species involved (*i*: H_2, O_2 and H_2O) can be found in CRC Handbook, [9] and with this is possible to compute x_{O_2}.

ii) Chemical potential can be then calculated by employing the following equations[10]:

$$\mu^o_{O_2(T)} = RT\left\{-1{,}225 - \frac{1045}{T} - 3{,}5\cdot ln(T) + 1{,}013\cdot ln\left[1 - exp\left(\frac{-2246}{T}\right)\right]\right\} \qquad \text{(S2)}$$

and,

$$\mu_{O_2(T_1,P_1)} = \mu^o_{O_2(T_1,P_1)} + RT_1\cdot \ln x_{O_2} \qquad \text{(S3)}$$

The table presented below summarizes the corresponding values of μ_{O_2} for the different conditions used at BESSY II, BElChem beamline, and the corresponding U_{cell} (Equation S1) associated with the E_b shift. In both cases T = 700 °C and total P = 0.5 mbar.

Atmosphere	x_{O_2}	μ_{O_2} **(kJ/mol)**	U_{cell} **(V)**
Oxidizing	0.2	-288.6	**1,1**
Reducing (50 % H_2)	5.2E-25	-727.7	

Hence, the obtained open circuit voltage $U_{cell} = 1.1\ eV$ is in good agreement with the detected E_b shift within the experimental resolution.

S4.2. Analysis of Sr and O profile

The Sr 3d spectrum of pristine STFN given in Figure S6 was obtained experimentally by hard X-ray photoelectron spectroscopy in Ultra High Vacuum (UHV) at ambient temperature using 6 keV photon energy at the BL15XU[11] beamline of the SPring-8 Synchrotron facility in Japan. The high photon energy helped to clearly resolve and distinguish the bulk doublet from the two surface doublets, which are broader than the bulk doublet due to the larger disorder (presumably due to different bond lengths and angles) that can occur at the surface compared to the periodic bulk.

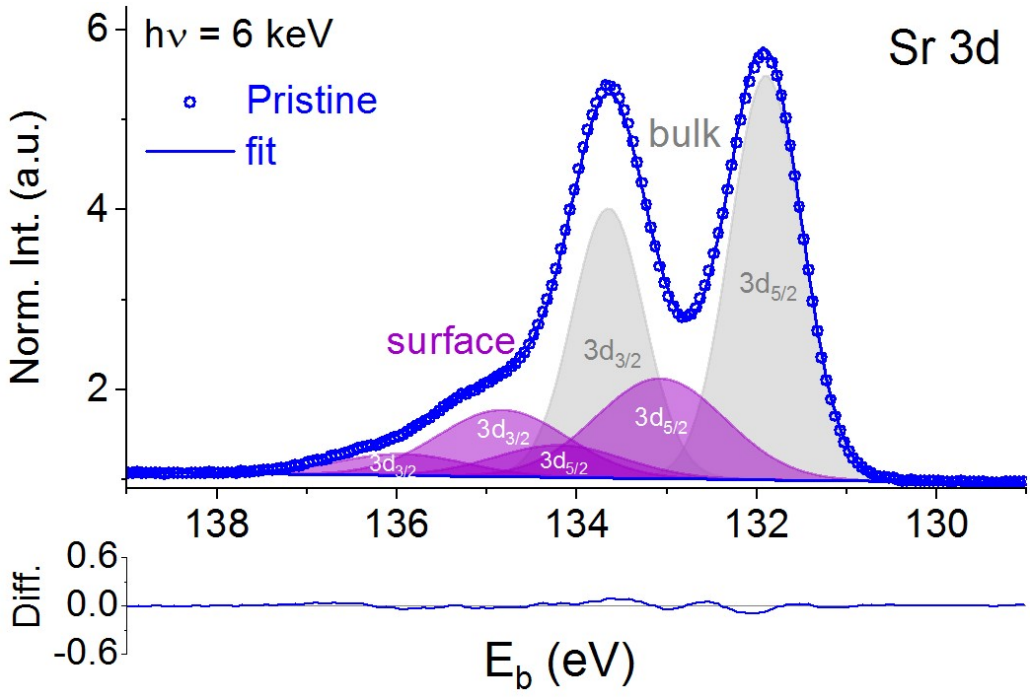

Figure S6. Sr 3d HAXPES spectrum of pristine STFN measured with 5670 eV photon energy by HAXPES.

Figure S7 shows the adopted models for fitting Sr 3d and O 1s NAP-XPS spectra of the STFN. The spectra were fitted with fityk[12] software, using Voigt functions and linear backgrounds. O 1s and Sr 3d spectra were fitted with a bulk and two surface species, as in references[8,13–15]. Sr $3d_{3/2}$ and Sr $3d_{5/2}$ components of each doublet had the same width, but allowing broader peaks for surface species as described for Figure S6, and a 2:3 area ratio to account for the 2j+1 multiplicity. The fitted doublet separation for all Sr 3d spectra was 1.77±0.03 eV, consistent with the 1.8 reported in the NIST database [16] and references [8,13–15].

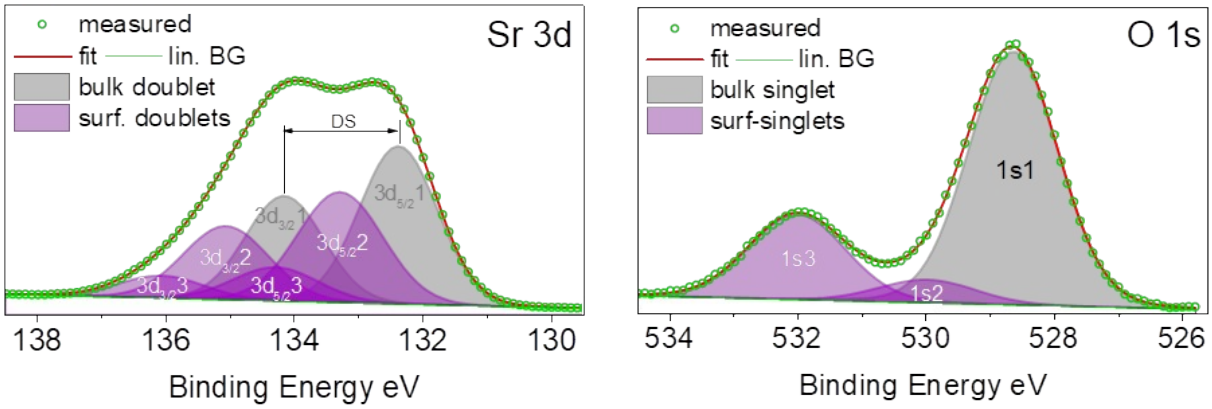

Figure S7. Models for fitting (a) Sr 3d and (b) O 1s spectra of STFN.

Figure S8 and S9 show the whole sets of in-situ acquired Sr 3d and O 1s fitted NAP-XPS spectra at 700 °C while redox cycling the atmosphere. The difference between measured and fitted intensities is plotted below each fitted spectra to show the goodness of the fits. The increasing kinetic energies of the probed photoelectrons of ca. 150, 400 and 700 eV correspond to IMFPs of about 0.5, 1.0 and 1.5 nm, respectively.[17] These values were estimated using the NIST database in reference [18], which relates the kinetic energy of the photoelectrons with the IMFP taking into account the material density (estimated as 5.27 g/cm^2), the number of valence electrons per molecule (estimated as 23.1 adding the contributions from the different chemical species in the sample) and the band gap energy (estimated as 2.115 from equation $E_g = 3.2 - 1.9x - 0.5x^2$ in reference [7], where x represents the Fe content in $SrTi_{1-x}Fe_xO_3$).

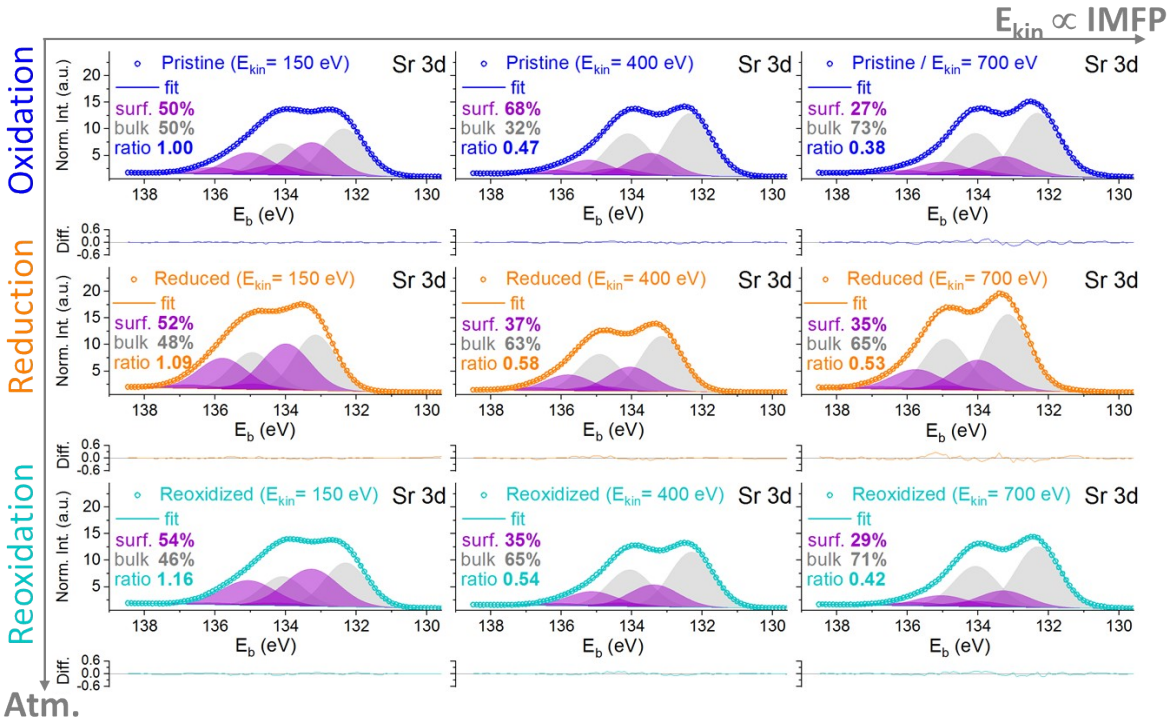

Figure S8. Whole fitted dataset of Sr 3d NAP-XPS spectra acquired in-situ at 700 °C for pristine, reduced, and reoxidized STFN, exploiting different kinetic energies for depth-dependent information.

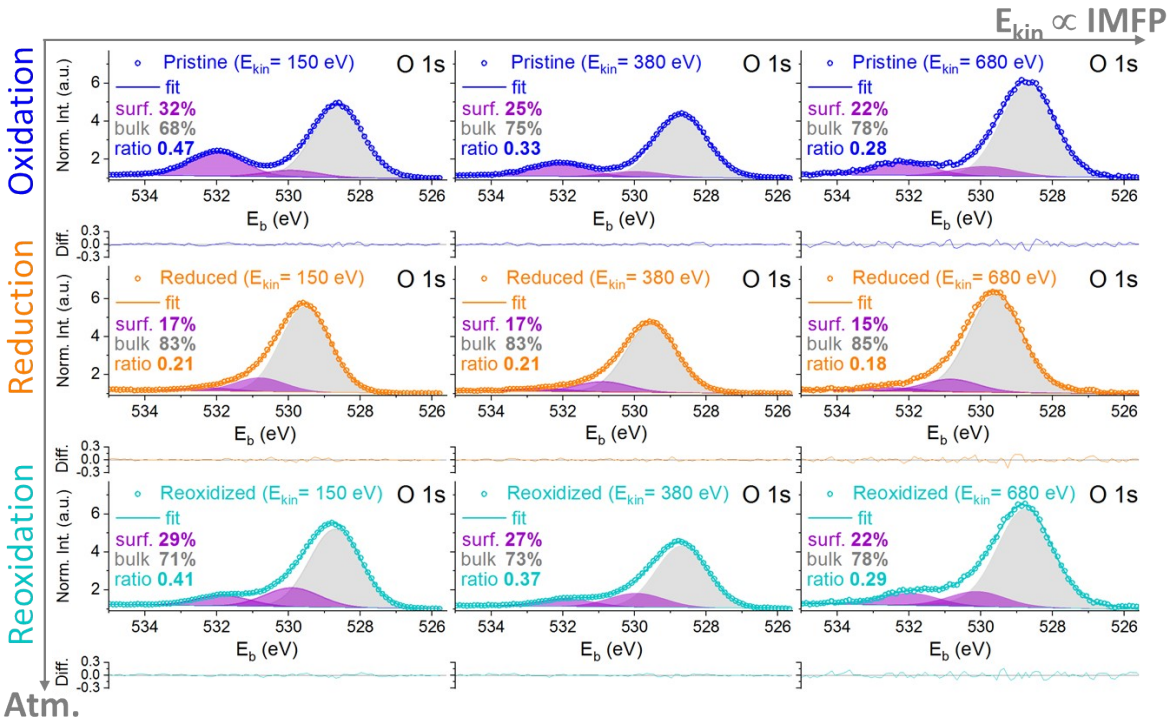

Figure S9. Whole fitted dataset of O 1s NAP-XPS spectra acquired in-situ at 700 °C for pristine, reduced, and reoxidized STFN, exploiting different kinetic energies for depth-dependent information.

Figure S10 shows the C 1s & Sr 3p core levels measured with 420 eV photon energy, at 700 °C in a complete redox cycle. Note that under these operation conditions no carbonaceous species are present.

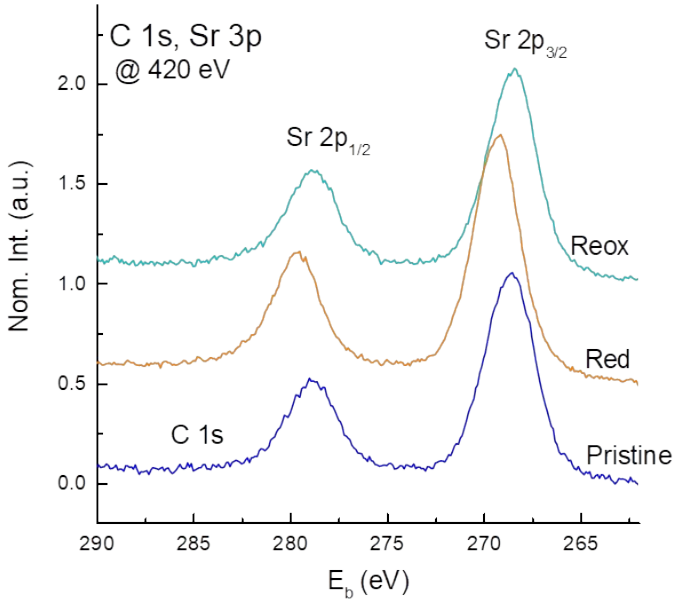

Figure S10. C 1s & Sr 3p spectra of the pristine, reduced, and reoxidized STFN pellet measured with 420 eV photon energy.

S4.3. Linear combination analysis

Figure S11 shows the XAS Fe L-edge spectra of the Fe foil, FeO and Fe_2O_3 references used for the Linear Combination Analysis (LCA). Both FeO and α-Fe_2O_3 have octahedral coordination, as is also expected for Fe in the perovskite structure studied. The FeO reference pattern was digitalized from reference [19]. The reference absorption spectra for Fe^0 and α-Fe_2O_3[20] were measured in total electron yield mode at the iRIXS endstation[21] of beamline 8.0.1 in the Advanced Light

Source, Lawrence Berkeley National Laboratory. The excitation energy was calibrated using the O K-edge XAS spectrum of TiO_2 powder.[22] The reference spectra were measured in UHV with excitation energy step size of 0.1 eV. Monochromator entrance/exit slits were 30µm/30µm, leading to a resolving power E/ΔE better than 5000.

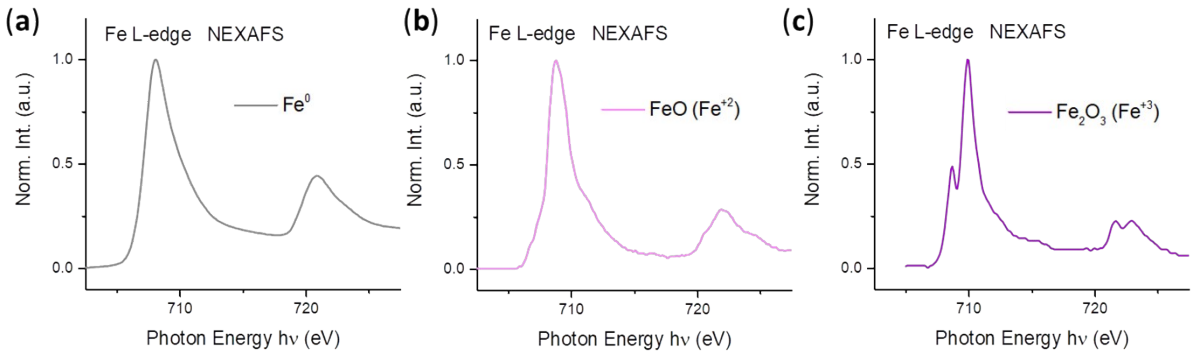

Figure S11. Fe L-edge XAS spectra of the (a) Fe^0, (b) FeO (Fe^{+2}) and (c) α-Fe_2O_3 (Fe^{+3}) used as reference for the Linear Combination Analysis (LCA).

References

1 M. Santaya, L. Toscani, L. Baqué, H. E. Troiani and L. Mogni, *Solid State Ionics*, 2019, **342**, 115064.
2 M. Hayase, M. Shiga and Y. Nakamura, *J. Phys. Soc. Japan*, 1973, **34**, 925–933.
3 A. R. Denton and N. W. Ashcroft, *Phys. Rev. A*, 1991, **43**, 3161–3164.
4 E. Barsoukov and J. R. Macdonald, Eds., *Impedance Spectroscopy*, Wiley, 2005.
5 S. B. Adler, J. A. Lane and B. C. H. Steele, *J. Electrochem. Soc.*, 1996, **143**, 3554–3564.
6 P. Hjalmarsson and M. Mogensen, *J. Power Sources*, 2011, **196**, 7237–7244.
7 A. Rothschild, W. Menesklou, H. L. Tuller and E. Ivers-Tiffée, *Chem. Mater.*, 2006, **18**, 3651–3659.
8 A. Nenning, A. K. Opitz, C. Rameshan, R. Rameshan, R. Blume, M. Hävecker, A. Knop-Gericke, G. Rupprechter, B. Klötzer and J. Fleig, *J. Phys. Chem. C*, 2016, **120**, 1461–1471.
9 J. Rumble, *CRC Handbook of Chemistry and Physics*, Taylor&Francis, 101st edn., 2020.
10 IUPAC, *Commission on Thermodynamics, Oxygen, International Thermodynamics Tables of the Fluid State-9*, Blackwell Sci., Oxford, 1987.
11 S. Ueda, Y. Katsuya, M. Tanaka, H. Yoshikawa, Y. Yamashita, S. Ishimaru, Y. Matsushita and K. Kobayashi, *AIP Conf. Proc.*, 2010, **1234**, 403–406.
12 Fityk, https://fityk.nieto.pl.
13 A. K. Opitz, C. Rameshan, M. Kubicek, G. M. Rupp, A. Nenning, T. Götsch, R. Blume, M. Hävecker, A. Knop-Gericke, G. Rupprechter, B. Klötzer and J. Fleig, *Top. Catal.*, 2018, **61**, 2129–2141.
14 Y. Wen, T. Yang, D. Lee, H. N. Lee, E. J. Crumlin and K. Huang, *J. Mater. Chem. A*, 2018, **6**, 24378–24388.
15 E. J. Crumlin, E. Mutoro, Z. Liu, M. E. Grass, M. D. Biegalski, Y.-L. Lee, D. Morgan, H. M. Christen, H. Bluhm and Y. Shao-Horn, *Energy Environ. Sci.*, 2012, **5**, 6081.
16 NIST Inorganic Crystal Structure Database (ICSD), https://srdata.nist.gov/xps/EngElmSrchQuery.aspx?EType=DS&CSOpt=Retri_ex_dat&Elm=Sr.
17 S. Tanuma, C. J. Powell and D. R. Penn, *J. Electron Spectros. Relat. Phenomena*, 1990, **52**, 285–291.
18 C. J. Powell and A. Jablonski, NIST Electron Inelastic-Mean-Free-Path Database, http://www.nist.gov/srd/surface.cfm.
19 T. Katayama, S. Yasui, T. Osakabe, Y. Hamasaki and M. Itoh, *Chem. Mater.*, 2018, **30**, 1436–1441.
20 K. D. Kwon, K. Refson, S. Bone, R. Qiao, W. Yang, Z. Liu and G. Sposito, *Phys. Rev. B*, 2011, **83**, 064402.
21 R. Qiao, Q. Li, Z. Zhuo, S. Sallis, O. Fuchs, M. Blum, L. Weinhardt, C. Heske, J. Pepper, M. Jones, A. Brown, A. Spucces, K. Chow, B. Smith, P.-A. Glans, Y. Chen, S. Yan, F. Pan, L. F. J. Piper, J. Denlinger, J. Guo, Z. Hussain, Y.-D. Chuang and W. Yang, *Rev. Sci. Instrum.*, 2017, **88**, 033106.
22 S. Roychoudhury, R. Qiao, Z. Zhuo, Q. Li, Y. Lyu, J. Kim, J. Liu, E. Lee, B. J. Polzin, J. Guo, S. Yan, Y. Hu, H. Li, D. Prendergast and W. Yang, *ENERGY Environ. Mater.*, 2021, **4**, 246–254.